The Commissioning of the Arcetri Near-Infrared Camera ARNICA: II. Broadband Astronomical Performance

L. Hunt[1], R. Maiolino[2], G. Moriondo[2], and L. Testi[2]
Infrared Group

Arcetri Technical Report, N° 3/1994

Firenze, November, 1994

[1] C.A.I.S.M.I.–C.N.R.
[2] Università degli Studi di Firenze

Contents

1 Introduction **1**

2 ARNICA's optics at the WHT and the TIRGO **1**

3 Optical performance **2**
- 3.1 Orientation of the focal plane array . . . 2
- 3.2 Plate scale and rotation angle . . . 4
- 3.3 Distortion . . . 5
- 3.4 Point spread function . . . 5
- 3.5 Focus with wavelength . . . 7
- 3.6 Ghosting . . . 8
- 3.7 Optical axis . . . 8

4 Throughput and sensitivity **8**
- 4.1 Dynamic range . . . 8
- 4.2 Efficiency . . . 9
- 4.3 Background . . . 11
- 4.4 Background-limited performance . . . 12
- 4.5 Sensitivity . . . 13

5 Spatial variation of photometric response during commissioning **14**
- 5.1 Empirical correction method . . . 15
- 5.2 Results . . . 15

6 Elimination of spatial variation of photometric response **17**
- 6.1 WHT, December, 1993 . . . 17
- 6.2 TIRGO, February, 1994 . . . 17

7 Results obtained with ARNICA **18**

8 Concluding remarks **20**

9 Acknowledgements **20**

1 Introduction

The Arcetri near-infrared (NIR) imaging camera, ARNICA, saw first light at the TIRGO almost two years ago, and both the camera and data acquisition system performed well from the start of the first commissioning campaign in November–December 1992. As a result, the first and subsequent commissioning runs of the camera have provided ample data by which to judge its astronomical performance.

This report is the second of a series that describes the data analysis and the quantitative results obtained with ARNICA. Our original intention was to limit this report to a description of ARNICA's performance during the commissioning of the camera at the TIRGO (November 1992 – June 1993). Various considerations have since induced us to also include a discussion of results obtained during an observing run in December, 1993, at the William Herschel Telescope (WHT, La Palma, Canary Islands), and during a subsequent observing run at the TIRGO (February, 1994).

In this report, we briefly describe the optical systems for ARNICA used at the TIRGO and the WHT. Optical performance during commissioning is evaluated in terms of distortion, spurious reflections ("ghosting"), and spatial variation of the point spread function. We assess the astronomical performance of the camera on the basis of instrumental throughput, sensitivity, and spatial variation of the photometric response. This report is concerned only with performance of the camera with broadband filters, as, during the commissioning campaigns, we were not able to acquire sufficient narrowband data to warrant performance assessment (see Gennari & Vanzi 1994). The magnitude calibration used throughout is based on observations of stars from the list of UKIRT faint standards kindly provided by C. Aspin.

2 ARNICA's optics at the WHT and the TIRGO

The original optical design for ARNICA at the TIRGO, and with which the camera was commissioned, is described in Lisi et al. (1993). Briefly, the system comprises two doublets: an achromatic collimator and the camera element. The filter wheel is placed at the pupil plane, between the two doublets. The pupil image in the original design was 5 mm in diameter, and there was a matched cold stop at the pupil plane.

At the WHT, the optical scheme comprises two triplets, and again, the filter wheel is placed at the pupil plane, between the two triplets. At the WHT the pupil image is 10 mm in diameter, and the optics do not contain a matched cold stop at the pupil plane.

Finally, for observing runs at the TIRGO starting in 1994, the matched cold stop at the pupil plane was eliminated. Therefore, the structural mounting for the lenses provides the only spatial constraint at the pupil plane. This alteration to

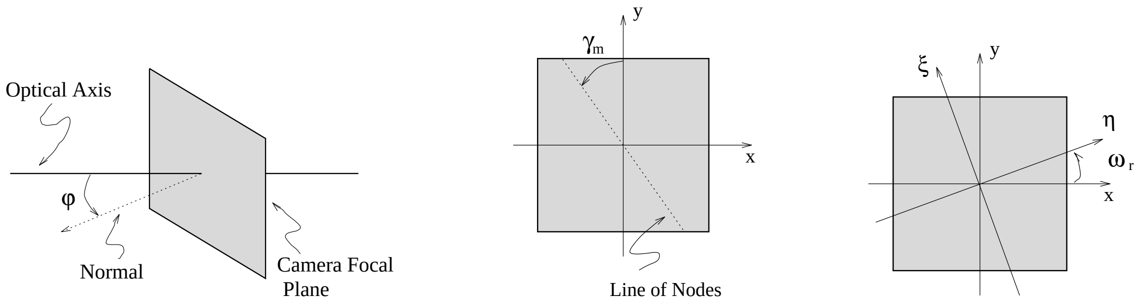

Figure 1: Sketch of the φ, γ_m, and ω_r angles that define the relative orientations of the focal planes of the camera and the telescope.

the original design was performed primarily to test our hypothesis, described below, about the cause of spatial variation of the photometry. In addition, initial design constraints that made a small pupil image imperative were no longer applicable.

3 Optical performance

3.1 Orientation of the focal plane array

In this section, we present an observational method to determine the geometry of the focal plane of the camera with respect to the focal plane of the telescope. In principle, the two focal planes should be coincident, with the pixels of the detector oriented along Right Ascension (RA) and Declination (DEC). Of course this cannot be accomplished with indefinite precision, and the relative orientations of the two focal planes should be determined *a posteriori*. Moreover, the scale on the detector (in arcsec pixel^{-1}) may not be the nominal one, due to imperfect optical components, misplacement of the array, or misalignment of the camera and the telescope. The parameters to be determined are: (i) the tilt angle φ, defined as the angle between the telescope and camera focal planes; (ii) the position angle γ_m, angle (positive counter-clockwise) between the *y-axis* on the array (after transposition) and the *line of nodes* (the intersection between the camera focal plane and the plane orthogonal to the optical axis that contains the array center); (iii) the (x_a, y_a) position (in *(x,y)* array coordinates) of the intersection between the optical axis and the camera focal plane; (iv) the *true* plate scale $\mathcal{S}$, that is the plate scale along the line of nodes; and (v) the angle ω_r (positive counter-clockwise) between the x-axis of the detector (after transposition) and the negative-RA axis. Angles φ, γ_m, and ω_r are sketched in Figure 1.

Clearly, if the focal planes of the camera and the telescope are misaligned, then the plate scale is a function of the position angle. The plate scale $s(\gamma)$ is related to the position angle γ with the formula:

$$\frac{1}{s^2(\gamma)} = \frac{\sin^2(\gamma - \gamma_m)}{\mathcal{S}^2 \cos^2(\varphi)} + \frac{\cos^2(\gamma - \gamma_m)}{\mathcal{S}^2} \quad (1)$$

where, as explained above, $\mathcal{S}$ is the *true* scale along the line of nodes.

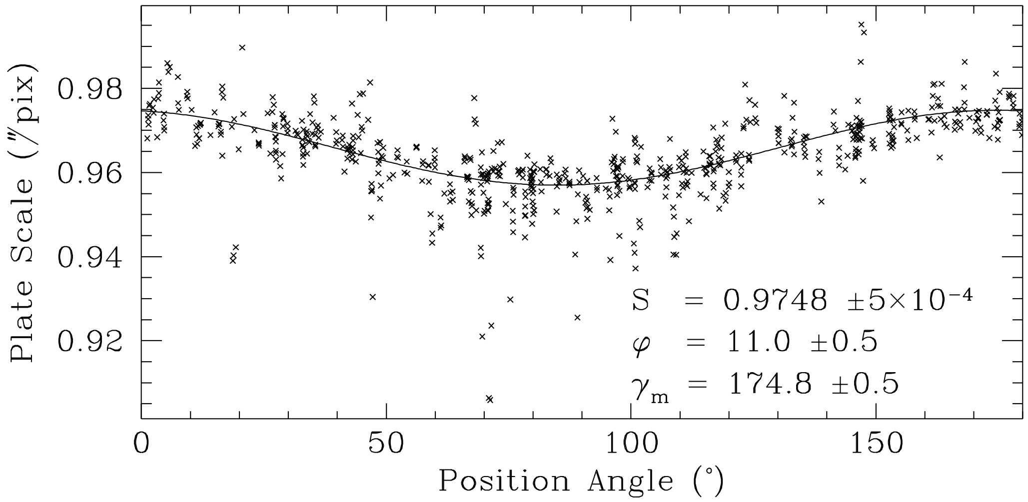

Figure 2: Fit for the plate scale as a function of the position angle. The crosses are the datapoints; the continous line is the best fit to the data. The parameters of the fit and their errors are reported.

From the Hubble Space Telescope Guide Star Catalogue (HST-GSC), we extracted the positions of a set of stars contained in fields observed with ARNICA. For each star we measured the (x, y) position on the array. For each pair of stars we determined the position angle γ and the plate scale $s(\gamma)$ measured for that pair. Using six fields in three different TIRGO runs observed in each of the three (J, H, and K) bands, we were able to measure 654 pairs of stars with a distance greater than 20 pixels on the array (shorter distances were excluded because they afford poor precision in the plate scale determination). On this data set we fit the curve given in Equation 1 using a non-linear least-squares technique. In Figure 2 the fit is shown as a continous line, while the data are represented by crosses.

The results of the fit are reported in Figure 2, with the relative uncertainties. The angles are given in degrees and the plate scale in arcsec pixel^{-1}. We note that with this model the sign of the tilt angle φ is indeterminate. We find that the angle between the camera focal plane and that of the telescope is $\sim$11°. This is most probably due to the non-telecentric configuration of the ARNICA optical system, combined with a possible error in the positioning of one of the lenses in the two doublets that make up the camera and collimator elements of the camera (see Lisi et al. 1993). An upper limit to the precision with which the array can be positioned relative to the camera optical axis is less than $\sim 1°$, so that this can be excluded as a possible cause of our result.

Applying the method outlined above to the data acquired with different filters separately, we can investigate the dependence of the plate scale with wavelength. Figure 3 shows the best fit to the data in the three wavebands. Within the precision achievable with this method, no dependence of the parameters with wavelength is found.

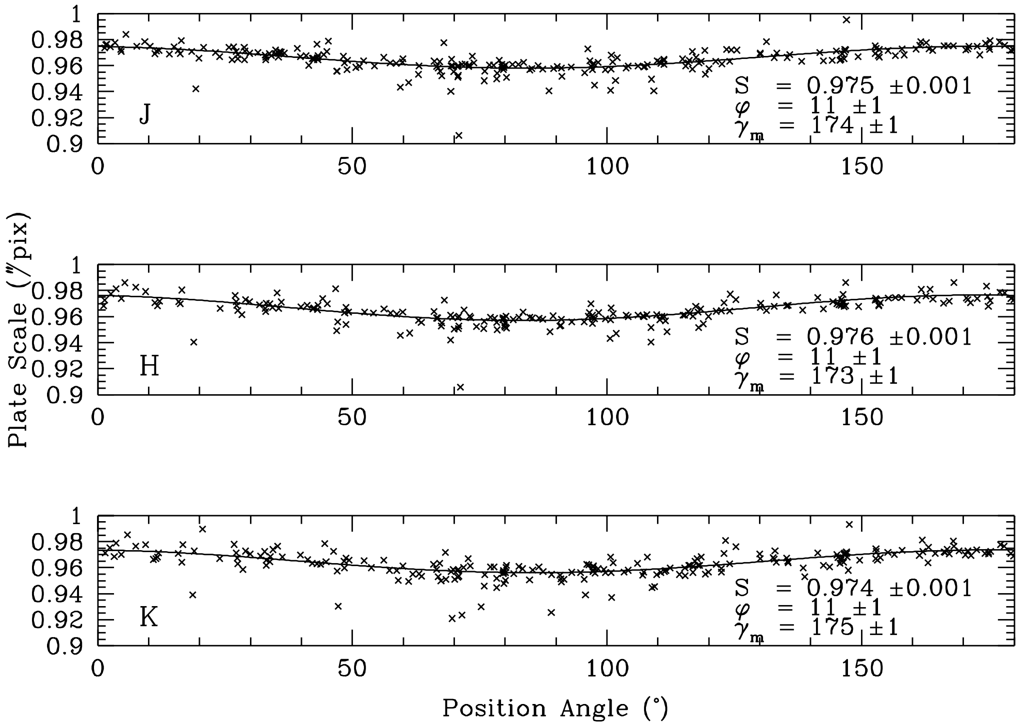

Figure 3: Fits for the three wavebands separately. The fitting parameters are reported in each panel.

3.2 Plate scale and rotation angle

Although the parameters derived up to now are very important in the characterization of the optical performance of the camera and should be carefully taken into account when deriving morphological parameters from the images, they are not the parameters that most of the observers will use during the analysis of their data. A typical observer would like to know the location of the RA and DEC axes on the array, and the value of the plate scale along these axes. These parameters will be briefly derived in the following.

Using the HST-GSC stars, it is possible to fit for the coordinate transformations between pixel and equatorial coordinates (see Testi 1993 for details). The results of the linear fit give the platescale in the array x- and y-axes, as well as the coupling between the two directions. We note that it is necessary to transpose ARNICA images acquired at the TIRGO (e.g., with IRAF task `imtrans`) to obtain the appropriate orientation (NE in the upper left corner). If (ξ,η) are the absolute equatorial coordinate offsets with respect to the reference point (ξ offsets are positive when RA decreases), then from the linear fit we obtain the coefficients C_{11}, C_{12}, C_{21}, and C_{22} defined by the equations:

$$\xi = C_{11}x + C_{12}y + \mathcal{O}_\xi(2); \qquad \eta = C_{21}x + C_{22}y + \mathcal{O}_\eta(2). \tag{2}$$

Neglecting the second-order terms ($\mathcal{O}_\xi$ and $\mathcal{O}_\eta$), we can derive the simple approximate relations between these coefficients and the plate scale along the ξ- and η-axis and the rotation angle ω_r defined in the previous section:

$$\begin{aligned} s_\xi &= s(\omega_r + 90°) = (C_{11}^2 + C_{12}^2)^{1/2}; \\ s_\eta &= s(\omega_r) = (C_{21}^2 + C_{22}^2)^{1/2}; \\ \tan(\omega_r) &= (C_{12}/C_{11} - C_{21}/C_{22})/2. \end{aligned} \tag{3}$$

Our measurements give the results:

$$s_\xi = 0.9581 \pm 0.0007; \qquad s_\eta = 0.9747 \pm 0.0007; \qquad \omega_r = -0.71 \pm 0.04. \tag{4}$$

The values of the plate scales along ξ and η are in excellent agreement with the values obtained from the fit of the previous section evaluating Equation 1 at $\gamma = \omega_r + 90°$ and $\gamma = \omega_r$:

$$s(\omega_r + 90°) = 0.9570; \qquad s(\omega_r) = 0.9746. \tag{5}$$

The mean values of the linear coefficients were found to be (the units of the coefficients are arcsec pixel^{-1}):

$$\begin{aligned} C_{11} &= 0.9579 \pm 0.0007; \quad C_{12} = -0.018 \pm 0.003; \\ C_{21} &= 0.0055 \pm 0.0006; \quad C_{22} = 0.9747 \pm 0.0007. \end{aligned} \tag{6}$$

In any case, astronomers who need accurate astrometry are encouraged to calibrate their own data.

3.3 Distortion

In the previous section we used a linear approximation to the transformation between pixels and equatorial coordinates. The amplitude of distortion in the optical system telescope+camera is determined by the degree to which this approximation is correct (and on which spatial scales).

To address this question, we used again the catalogue stars and solved the transformation equations, this time including the second-order terms:

$$\begin{aligned} \mathcal{O}_\xi(2) &= Q_{11}x^2 + Q_{12}y^2 + Q_{13}xy; \\ \mathcal{O}_\eta(2) &= Q_{21}x^2 + Q_{22}y^2 + Q_{23}xy. \end{aligned} \tag{7}$$

The values of the Q_{ij} terms in our solutions show a large scatter, without any clear trend. Nevertheless, the absolute values of these coefficients are always three or four orders of magnitude smaller than the C_{ii} coefficients. This result implies that the distortion terms can be important and should be taken into account when comparing the positions of stars at the opposite edges of the detector, as the non-linear correction can approach 10% in some cases. On small scales ($\lesssim$ 100 pixels), the linear approximation should be correct within 1%.

3.4 Point spread function

To look for spatial variations of the width of the point-spread function (PSF), we used the same kind of data that were used to determine the spatial variation in the

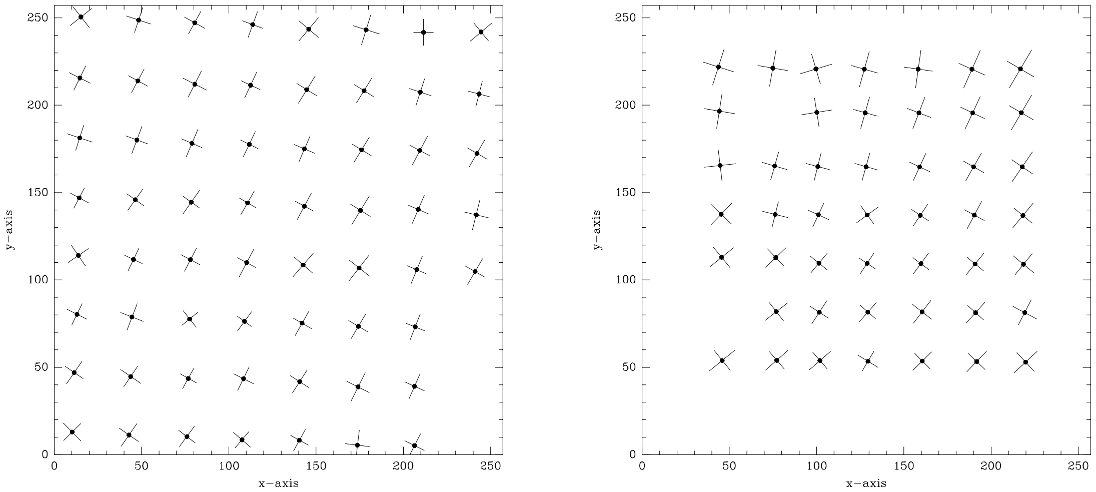

Figure 4: Spatial variation of the fitted PSF σ-width and position angle for the telescope data of December, 1992 (left panel) and for the laboratory data of May, 1993 (right panel).

photometry (see §5). These data consisted of a set of frames of a point-like source placed in a regular grid of positions on the array. We analyzed two such data sets, the first obtained at the TIRGO telescope in December, 1992 and the second in the laboratory in May, 1993. At the telescope we used a star, and in the laboratory we used the image of an optical fiber and the lens system that simulates the TIRGO beam (SimulTIRGO). At the telescope, we analyzed data in all three broad bands, while in the laboratory, only the J-band is available.

After flat-fielding the images (see §5), the PSF in each position was fitted with an elliptical cross-section gaussian using the IRAF[1] task FITPSF which provides the σ-width along major and minor axes, center coordinates, the peak-amplitude, and the position-angle. The fitted PSF's are reported in Figure 4. In the figures, the PSF is represented by a cross with bars whose lengths are proportional to the σ-widths of the PSF, and whose position angle gives the orientation.

Visual inspection of the right panel of Figure 4 shows a definite trend in the PSF σ-width, with larger images near the top edge of the detector. This behavior is almost certainly due to a misalignment (discovered *a posteriori*) between the optical axes of the camera and the SimulTIRGO. The mean difference in area of 25% is too large to be explained only by the tilt angle φ determined in the previous section, which should produce a difference of only 2% (and present azimuthal symmetry relative to the optical axis if the camera and SimulTIRGO are aligned).

Instead, data obtained at the telescope look quite uniform (left panel of Figure 4), and the spread of the PSF is in practice independent of position. We argue that seeing effects dominate at the telescope, hiding the off-axis enlargement of the

[1]IRAF is the Image Analysis and Reduction Facility, made available to the astronomical community by the National Optical Astronomy Observatories, which are operated by AURA, Inc., under contract with the U.S. National Science Foundation.

Table 1: Secondary mirror positions in the J, H and K wavebands

Date	J pos.	H pos.	K pos.	ΔJ–H pos.	ΔH–K pos.
29/30 Sep 1993	1490 ± 3	1500 ± 3	1520 ± 3	10	20
12/13 Feb 1994	1600 ± 3	1620 ± 3	1640 ± 3	20	20
10/11 Sep 1994	1510 ± 3	1515 ± 3	1525 ± 3	5	10

PSF; hence systematic variations across the field of view are not detectable. The alignment of most of the position angles in Figure 4 (which is not observed for laboratory data) is most probably due to a slight error in the telescope tracking on timescales of a minute or so (the length of the acquisition time of the images).

The specifications of the original optical design require that in a circle of diameter 4 arcmin centered on the optical axis one pixel contains 80% of the total encircled energy, and at the vertices more than 70%. This corresponds to a difference in the width of the PSF of roughly 20μm (0.5 pixel) in all three broad bands. Neither of the two data sets analyzed are sufficient to detect this difference.

3.5 Focus with wavelength

In general the determination of the optimum focus and its dependence on wavelength is not easy. At present, focussing is performed manually, with the camera in continuous acquisition mode, by minimizing the area (or width) of a stellar image. We discuss here *average*, *empirical* determinations of the difference between the secondary mirror position for different wavebands, assuming that all other conditions are similar (e.g., temperature and zenith angle of the telescope). Table 1 reports the secondary mirror positions and their differences (in units of arbitrary motor *steps*) for three nights.

Although a large scatter is observed, it is possible to conclude that the difference in focus position between the J and H band is roughly 10 motor steps, while between H and K is roughly 15 steps. Because of the large uncertainty, using these values without verification is not advisable.

ARNICA's original optical design foresees a defocus between the K- and the J-bands of 0.9 mm. With a secondary mirror step corresponding to 5μm, this implies a much larger difference in wavelength than is observed. However, because of the sub-pixel dimensions of the intrinsic PSF, the PSF observed at the telescope is dominated by effects of telescope misalignment, thermal gradients across the primary mirror, and secondary mirror support problems (Esposito et al. 1993). Hence, the empirical differences in secondary position as a function of wavelength are attributable to these and not to the defocus in the camera's optical design.

3.6 Ghosting

To assess the amplitude of multiple reflections ("ghosts") from ARNICA's internal optics, we analyzed two kinds of images. The first, acquired at TIRGO during commissioning, consists of spurious reflections associated with bright overexposed stars in the three broadband filters, J, H, and K. The second set of images was obtained with the J filter in the laboratory with an optical fiber and SimulTIRGO.

The TIRGO images of bright stars were acquired in January, 1993, and comprise three Herbig Ae/Be fields. We performed photometry of the ghosts with the `phot` routine in IRAF, employing manual centering because of the irregular form of the ghosts, a virtual aperture of 12 arcsec, and the background determined in a concentric annulus. The magnitude calibration was performed as described in §4.3. All of the central stars were saturated, so it was not possible to perform accurate photometry. Instead, we used magnitudes from the literature for the central stars (Hillenbrand et al. 1992). We find that the amplitude of the ghosts is largest in the J-band, ranging from 1.4% to 1.7%. In the H-band, the amplitude is 0.7%, and in the K-band, the amplitude is the smallest, ranging from 0.4% to 0.6%.

The result for the J-band is confirmed by the laboratory tests, where the amplitude of the spurious reflections from the optical fiber image is $\leq 2\%$.

The trend with wavelength, that is decreasing amplitudes of the ghosts with wavelength, is probably explained by systematic differences in the reflectivity of the array and the surfaces of the filters. In any case, problems with ghosts have been ameliorated as of 1994 by tilting the filters with respect to the optical axis.

3.7 Optical axis

We used ghosted images to define the position of the optical axis on the array. These images were acquired in January, 1993, and so give an estimate pertaining only to the runs with ARNICA until October, 1993, when the optical train was disassembled for the observing run at the WHT. Using five different cases with clearly identifiable ghosts, we found an (x_a, y_a) position of (121,135) (transposed) $\pm\ \sim 3$ pixel. Such a relatively large error is due to the low precision with which we determine the center of the ghosts, as their form is highly irregular. The positions of the optical axis in the three different broad bands, J, H, and K, are indistinguishable to within the measurement error.

4 Throughput and sensitivity

4.1 Dynamic range

Assuming a read noise of 50 e^- (Hunt et al. 1994a, hereafter Report I), the minimum level of ADU (analog-digital units) should be $\gg 125$, so that the measurement is not dominated by read noise (Hunt et al. 1994b, hereafter Report III). Without applying a non-linearity correction, the maximum reliable ADU level before which saturation sets in is roughly 12000–13000 ADU. Over this range, that is from roughly some hundreds of ADUs to 13000, the detector is linear to within 1.5% (Report I). Therefore, without correcting for linearity, signals that differ by a factor of about 100 in intensity can be reliably observed in the same exposure. Applying a correction for the intrinsic non-linearity of the detector (e.g., Report I) gives a maximum reliable ADU level of 15000 ADU, performance linear to 0.3%, and a dynamic range of a factor of something like 120.

4.2 Efficiency

We present here a derivation of the formulae we used to define the efficiency of the camera, that is to say the ratio of photons impinging on the atmosphere to photo-electrons detected by the camera's focal plane array. The magnitude of a point source is defined to be:

$$m_* = -2.5 \log \left(\frac{f_*}{f_0} \right) \tag{8}$$

where f_* is the total point-source monochromatic flux density in units of erg cm^{-2} s$^{-1}\mu$m^{-1} and f_0 is the monochromatic flux density of a source with zero magnitude. Observing point sources of known magnitudes give the zero point, defined to be (see Henden & Kaitchuck 1982):

$$ZP = m_* + 2.5 \log f_* = 2.5 \log f_0 \tag{9}$$

We note that here ZP is in physical units, and not in the instrumental units of ADU (analog-to-digital units, or counts).

An expression for the integrated (over the area on which the point source impinges) counts from a point source can be written as:

$$A_* = \eta \Delta\lambda \frac{\pi}{4} D^2 (\Sigma\phi_s) G \tag{10}$$

where A_* is in units of ADU/s, η is the total throughput in units of e$^-$/photon, $\Delta\lambda$ is the bandpass of the filter, D is the effective diameter of the telescope (corresponding to the collecting area), $\Sigma\phi_s$ is the integrated photon flux density from the source, and G is the conversion factor, or gain, in units of ADU/e$^-$. The monochromatic flux density from a point source in units of erg cm^{-2} s$^{-1}\mu$m^{-1} can be expressed as:

$$f_* = (\Sigma\phi_s) h\nu \tag{11}$$

where h is Planck's constant, and ν is the central frequency of the bandpass. From the absolute calibration of the magnitude scale, we can therefore relate f_* to the observed integrated flux density A_*:

$$f_* = \frac{A_*}{G\eta\Delta\lambda\frac{\pi}{4}D^2} \tag{12}$$

and express the ZP as a function of A_*:

Table 2: Absolute calibration and filters used for efficiency calculation

Filter	f_0 (Jy)	λ (μm)	$\Delta\lambda$ (μm)
J	1560	1.25	0.3
H	1030	1.65	0.3
K	645	2.2	0.4

Table 3: ARNICA's efficiency from 1992 to 1994

Observing run	Date	$\eta_{\rm J}$	$\eta_{\rm H}$	$\eta_{\rm K}$
TIRGO	December, 1992 – March, 1993	0.08	0.25	0.23
WHT	December, 1993	0.17	0.34	0.33
TIRGO	February, 1994	0.15	0.29	0.30

$$ZP = m_* + 2.5 \log \frac{A_* h\nu}{G\eta\Delta\lambda\frac{\pi}{4}D^2} \qquad (13)$$

Solving for η gives the efficiency or throughput as a function of observed and known quantities:

$$\eta = \frac{A_* h\nu}{f_0 \ \mathrm{dex}\ (-0.4 m_*)\ G\Delta\lambda\frac{\pi}{4}D^2} \qquad (14)$$

If f_0 is given in Jy, and ZP is in the instrumental units of ADU, the efficiency η can be written as:

$$\eta = \frac{h \ \mathrm{dex}\ [0.4\ ZP(\mathrm{ADU})]}{f_0(Jy)\ 10^{-23}\ \frac{\Delta\lambda}{\lambda}G\frac{\pi}{4}D^2} \qquad (15)$$

where λ is the central wavelength of the filter. To calculate the efficiencies quoted here, we have used the mean of two absolute calibrations in the NIR (Campins et al. 1985, Wilson et al. 1972), which correspond to the Arizona and CalTech photometric systems, respectively. These values, together with the bandpasses and central wavelengths, are given in Table 2.

From observations of standard stars, we were able to calculate the efficiency of ARNICA during the commissioning runs (December, 1992 – March, 1993), during the run at the WHT (December, 1993), and during a subsequent observing run at the TIRGO (February, 1994). These values are given in Table 3. We note that η derived as described above comprises losses from the atmosphere, the telescope, as well as the camera.

Initial problems with alignment made the efficiency of the camera during commissioning lower than that found during the WHT run and subsequent observing

Table 4: Observed backgrounds

Observing run	Date	J (e^- s^{-1} arcsec^{-2}) (mag arcsec^{-2})	H (e^- s^{-1} arcsec^{-2}) (mag arcsec^{-2})	K (e^- s^{-1} arcsec^{-2}) (mag arcsec^{-2})
TIRGO	December, 1992 – March, 1993	1000 – 1300 14.7 – 15.0	6000 – 8700 12.8 – 13.2	4000 – 6400 12.6 – 13.2
WHT	December, 1993	8400 15.5	59200 13.4	150000 11.8
TIRGO	February, 1994	1500 – 3000 14.5 – 15.5	8800 – 10000 12.5 – 13.5	4700 – 6800 13.0 – 13.5

runs at the TIRGO. The camera's efficiency during the TIRGO February, 1994 run is comparable to that achieved at the WHT.

4.3 Background

The amplitude of the background and the accuracy with which it can be measured dictate the dynamic range (§4.1) that can be reached in practice for weak point sources and for extended sources. We report in Table 4 the background observed at the TIRGO both before (during commissioning) and after the removal of the cold stop at the pupil plane, together with that observed at the WHT. The conversion to e^- was performed using 20 e^-/ADU (Report I). The magnitude calibration was achieved with nightly observations of several standard stars.

The background levels measured with ARNICA at La Palma are similar to those measured at Las Campanas by Persson et al. (1992), and show a rather bright K-band background relative to that measured in the J- and H-bands. The TIRGO background is brighter than that at the WHT in J and H, and is similar to that reported by Rieke et al. (1987); in the K-band, the background level at TIRGO is roughly a magnitude fainter than those reported by Persson et al. and Rieke et al., probably because the TIRGO is a telescope optimized for infrared work and situated at a cold site.

It is of interest to note the background levels at the TIRGO and the WHT with the different sets of optics. As mentioned before, at the TIRGO for the February, 1994 run, the matched cold stop was eliminated. Comparing the entries in Table 4 shows that the background without the matched cold stop is comparable to if not less than that with the stop in place. Although in principle the cold stop at the pupil plane of the camera reduces the background arriving at the detector, the observed values of the background with and without the stop strongly suggest that, with a short-wavelength cutoff detector such as the NICMOS HgCdTe array and a relatively cold telescope, such a stop is unnecessary.

4.4 Background-limited performance

The best-quality images, that is the highest signal-to-noise values for each pixel, are provided by working in a background-limited regime. This is ensured by setting on-chip integration times long enough so that the photon noise due to the background dominates the noise; in the case of ARNICA with a low dark current detector, the statistical noise should be much larger than the read noise, $\sim$50 e^- (Report I).

The assumption that an image is, indeed, background limited can be checked by correctly propagating the errors introduced by data reduction and comparing the theoretical noise expected to that observed. We provide here a simple formula for the noise expected from background-limited performance. See McCaughrean (1988) or Hunt (1993) for a complete derivation. Taking into account the division by a flat-field, and assuming that the error on the (scalar) sky subtraction is negligible, the noise per pixel in e^-/s/pixel for a coadded image can be written as:

$$\sigma_e = \sqrt{\frac{F_B\left(1 + \frac{M_S}{M_B}\right)}{T_{tot}}} \tag{16}$$

where F_B is the background count rate in e^-/s/pixel, M_S and M_B are the number of coadded source and flat-field frames, respectively, and T_{tot} is the total exposure time, that is the product of the on-chip integration time and the number of frames coadded together. Converting this expression into ADU/s/pixel gives:

$$\sigma_A = \sqrt{\frac{GA_B\left(1 + \frac{M_s}{M_B}\right)}{T_{tot}}} \tag{17}$$

where A_B is the background count rate in ADU/s/pixel, and G is the gain conversion factor (ADU/e^-).

To be sure that no noise was systematically introduced by the read-out or data acquisition, we spot checked ARNICA images to make sure that, indeed, they were background limited. The spatial standard deviation over small numbers of pixels in empty zones of the images was calculated with the IRAF procedure, `imexamine`. All of the images for which we compared the noise predicted with Equation 17 to that observed were background limited.

A caveat is necessary, however. Equation 17 is applicable to *coadded* or single images. When flat fields or images after registering are combined using a median algorithm with bad-value clipping, the resulting spatial noise does not scale with integration time in the same way as a simple average. Experience has shown that such a method results in scaling with an *effective* integration about 2/3 that of the actual time elasped (see Carter 1993 and Hunt et al. 1994b, hereafter Report III).

Table 5: Point- and extended-source limiting magnitudes

Observing run	Date	J	H	K
TIRGO commissioning	December, 1992 – March, 1993			
Extended sources	(mag arcsec^{-2}, 3σ, 60s)	19.1 – 19.3	18.1 – 18.3	17.8 – 18.0
Point sources	(mag, ϕ=3 arcsec, 3σ, 60s)	17.8 – 18.2	17.1 – 17.3	16.7 – 16.9
WHT	December, 1993			
Extended sources	(mag arcsec^{-2}, 3σ, 60s)	19.9	18.9	18.0
Point sources	(mag, ϕ=1.5 arcsec, 3σ, 60s)	20.7	19.7	18.8
TIRGO	February, 1994			
Extended sources	(mag arcsec^{-2}, 3σ, 60s)	19.3 – 19.7	18.5 – 18.6	18.3 – 18.5
Point sources	(mag, ϕ=3 arcsec, 3σ, 60s)	18.2 – 18.6	17.4 – 17.5	17.2 – 17.4

4.5 Sensitivity

Camera sensitivity was derived from observations of point-like and extended sources. At the TIRGO, we used sky frames to apply the flat-field correction; for point sources, the flat field for each image was a combination of all frames except the one to be corrected, and for extended sources the flat field for each image was the average of the pair of sky frames taken before and after the source frame. At the WHT, in J and H the flat-field correction was applied using sky frames as for the TIRGO observations. Instead, in K, sky frames as calculated above were subtracted (instead of divided), and differential dome flats were used for the flat-field correction. Further details of data acquisition and reduction are given in §5 and in Report III.

We report the limiting magnitudes calculated from the observed noise values in Table 5. The point-source sensitivity is derived assuming a circular aperture of diameter dictated by the seeing conditions, and denoted in the table by "ϕ". The observed limiting point-source magnitudes quoted in the table are *detection limits*; the photometric limit, or the brightness of the sources for which photometry can be reliably performed (10σ, $\phi_{\mathrm{phot}} \geq 3\phi$), is ≥ 2.5 mag fainter.

Two requirements are implicit in the sensitivities given in the tables: the first is background-limited performance, and the second is an adequate flat-field correction. When sky frames are used for the flat-field correction, images acquired with ARNICA are typically flat to within 0.1% or better. With appropriate data acquisition and reduction techniques, the noise over large spatial scales, or "flatness", is negligible with respect to the high spatial frequency noise arising from the statistical fluctuations of the signal collected on each pixel. In other words, the noise characteristics over an entire row or column of the array are comparable to those over a small region or even for a single pixel of the detector. The limiting magnitudes quoted in the tables assume that the amplitude of residual trends over large spatial scales is negligible relative to the pixel-to-pixel noise due to photon statistics. It is important to realize that integration times cannot be made arbitrarily long to improve signal-to-noise, since the flat field correction cannot be performed arbitrarily well.

Table 5 shows that the point-source sensitivities measured at the WHT and the TIRGO scale with telescope area in the J- and H-bands. In contrast, the K-band performance of ARNICA at the WHT is worse by almost a magnitude than that expected from simple scaling. We attribute this to the higher background level at the WHT (see Table 4), presumably due to the more highly emissive telescope structure (that also necessitated the differential flat data reduction technique described below).

5 Spatial variation of photometric response during commissioning

During the commissioning runs, we used generally two modes for the acquisition of photometric data. Each night and in each filter, once every hour or so, a standard star was observed in five positions on the array, sampling each quadrant of the array and a near-central point. In addition, for each waveband at least once during the run, a standard star was placed in 64 positions on the array, forming a regular 8×8 point grid. The latter mode of data acquisition was aimed at testing the spatial uniformity of point-source photometry, while the former at sampling the photometric quality of the night.

The standard star sequences were reduced by first applying a flat field correction; the flat field for each of the images was constructed by combining a set of the remaining frames in the sequence with a median filter and rigorous clipping algorithm. For the 5-position scans, the four images with the star in different positions were combined for the flat field. For the 64-position scans, the flat field was constructed by combining the five frames acquired before and after the position of interest. We note that the double-sampling read-out algorithm and the negligible dark current make bias and dark current subtraction unnecessary. As mentioned below, the subtraction of a sky frame before the flat field correction did not improve the variation in the photometry.

After flat-fielding each of the standard star images, virtual (software) aperture photometry was performed by automatically centering on the stellar image and integrating over a 10-arcsec (in radius) aperture, with the sky subtraction determined from an 8-arcsec (in radius) annulus with an inner radius of 12-arcsec. Data reduction was accomplished with the ARNICA software package in the IRAF environment; details are discussed in Report III.

Photometric results in all three broad bands (J, H, and K) obtained both from the 5-position scans and the 8×8 grids were disappointing. The magnitude of the photometric spatial variation ranged from 10 to 20%, and was, in some cases, as high as 2 mag peak-to-peak over the entire array. Variations (standard deviations) of the photometry with position were always measurably larger than the variations in a single position. We discovered, however, that the spatial variation of the photometry was reproducible, as the discrepancies were the same from night to night during a given run. As long as the orientation of the camera relative to the telescope remained fixed, the pattern of the spatial variation of the photometry remained stable. Moreover, laboratory tests in June, 1993 with SimulTIRGO confirmed the presence of spatial variation of photometric response. We therefore ruled out the telescope or the atmosphere as possible causes. Moreover, although correction for bad pixels ameliorated the variation, it remained; it was also impossible to eliminate it by subtracting a sky frame before the flat-field correction.

5.1 Empirical correction method

After some experimentation, we developed a technique to correct for the observed spatial variation in the photometry. After normalization to the mean of the photometry, the 8×8 grids of standard star observations were bilinearly interpolated to create a 256×256 image, then fit with second-degree Chebychev polynomials. This procedure results in a fitted surface that corresponds to the deviation relative to the average response. The fitted surface was divided into the original images after the flat-field correction and scalar sky subtraction (subtraction of the image median), and virtual-aperture photometry was performed as before. This process was repeated for each waveband.

5.2 Results

After application of the corrective surface, the spatial variation of the photometry improved drastically. Standard deviations with position of 0.10–0.15 mag were decreased typically by factors of two or more; in one case, the reduction was a factor of five. Table 6 presents zero points and their variation for the commissioning runs, both before and after application of the corrective surface. We defined the intrinsic photometric quality of the night, given in Col. (4), as the average variation at a single position. It can be seen from the table that after correction (Col. (6)) the spatial variation of the photometry over the array is equal to or less than the nightly photometric quality. In spite of the initial spatial variation in the photometry, the final precision with which we could perform accurate photometric measurements with ARNICA approaches that achievable with single-element detectors, commensurate with the photometric quality of the observing night.

Unfortunately, application of the corrective surface introduces low-frequency spatial gradients, thus worsening the flatness of the processed image. Before application of the photometric surface, images reduced with the techniques described above are typically flat to within 0.1%. This figure can be degraded after application of the correction by as little as 10% to as much as 25 or 30%. Such degradation may be a problem for the detection of faint extended sources; in this case, though, elevated photometric precision is usually not an issue so that use of the corrective surface would be unwarranted.

Table 6: Photometry before and after corrective surface

Date	Band	No. stars	Intrinsic	Uncorrected	Corrected
(1)	(2)	(3)	(4)	(5)	(6)
23/24 Dec 92	J	3 (15)	0.06	19.02 ± 0.10 (0.07)	19.06 ± 0.08 (0.04)
	H	3 (14)	0.15	19.15 0.18 (0.10)	19.26 0.16 (0.05)
	K	3 (14)	0.08	18.74 0.10 (0.07)	18.74 0.07 (0.03)
24/25 Dec 92	J	2 (10)	0.03	19.27 ± 0.07 (0.06)	19.31 ± 0.05 (0.04)
	H	2 (10)	0.05	19.38 0.08 (0.08)	19.49 0.05 (0.04)
	K	6 (30)	0.06	18.89 0.10 (0.08)	18.89 0.06 (0.03)
25/26 Dec 92	J	7 (34)	0.05	19.28 ± 0.06 (0.04)	19.33 ± 0.05 (0.02)
	H	8 (39)	0.06	19.39 0.08 (0.05)	19.50 0.06 (0.02)
	K	8 (39)	0.08	18.95 0.09 (0.05)	18.94 0.08 (0.03)
26/27 Dec 92	J	6 (30)	0.06	19.31 ± 0.08 (0.07)	19.32 ± 0.06 (0.05)
	H	6 (30)	0.05	19.39 0.11 (0.09)	19.47 0.08 (0.03)
	K	5 (25)	0.08	18.94 0.14 (0.12)	18.90 0.12 (0.06)
28/29 Dec 92	J	3 (15)	0.10	19.34 ± 0.15 (0.11)	19.35 ± 0.14 (0.09)
	H	3 (15)	0.08	19.36 0.12 (0.11)	19.44 0.08 (0.04)
	K	3 (15)	0.11	18.89 0.14 (0.10)	18.89 0.10 (0.02)
11/12 Feb 93	J	2 (9)	0.08	19.23 ± 0.09	19.23 ± 0.07 (0.05)
	H	1 (4)	0.02	19.25 0.06	19.31 0.02
	K	5 (23)	0.05	18.74 0.10 (0.10)	18.76 0.05 (0.04)
13/14 Feb 93	J	5 (18)	0.04	19.24 ± 0.07 (0.06)	19.25 ± 0.06 (0.04)
	H	5 (20)	0.08	19.24 0.09 (0.05)	19.26 0.08 (0.02)
	K	4 (14)	0.09	18.72 0.10 (0.08)	18.73 0.09 (0.04)
14/15 Feb 93	J	7 (30)	0.04	19.24 ± 0.08 (0.07)	19.26 ± 0.06 (0.05)
	H	7 (30)	0.03	19.23 0.08 (0.08)	19.26 0.05 (0.05)
	K	6 (25)	0.08	18.71 0.10 (0.08)	18.75 0.08 (0.03)
16/17 Feb 94	J	4 (20)	0.05	19.66 ± 0.08 (0.05)	–
	H	3 (15)	0.06	19.62 0.07 (0.04)	19.62 ± 0.06 (0.03)
	K	3 (15)	0.07	19.13 0.08 (0.05)	19.14 0.08 (0.06)
17/18 Feb 94	J	2 (10)	0.03	19.67 ± 0.04 (0.04)	–
	H	2 (10)	0.04	19.60 0.06 (0.05)	19.61 ± 0.06 (0.05)
	K	2 (8)	0.04	19.20 0.07 (0.06)	19.23 0.07 (0.06)

Notes to Table 3:
Col. (1): Date of observations.
Col. (2): Filter.
Col. (3): Number of stars observed. The number for the mean and standard deviation given in Cols. (5) and (6), that is the product of the number of stars observed times the number of positions (typically five) of the star on the array, is given in parentheses.
Col. (4): Intrinsic photometric quality of the night as determined from the mean, over all positions, of the standard deviation of all the measurements at a single position.
Col. (5): The mean zero point and standard deviation, over all stars in all positions, before application of the corrective surface. The standard deviation of the position means (typically five) is given in parentheses, and would be the formal error to be associated with the photometry in a combined image.
Col. (6): As in Col. (5), but after application of the corrective surface.

6 Elimination of spatial variation of photometric response

As will be described below, the empirical solution to the spatial variation of ARNICA's photometry was superseded by a slight alteration in the optical design. Observations acquired after January, 1994 do not present the spatial variation described above.

6.1 WHT, December, 1993

At the WHT (December, 1993), with a different set of camera optics (see §2) and with data reduction as described above, spatial variation of the photometry in J and H was comparable to the nightly photometric quality (2–3% standard deviation). In the K-band, the situation was different, as the use of sky frames for the flat field correction resulted in photometric spatial variation around 8–10% (standard deviation).

The WHT K-band photometry required a different method of data reduction than that used in the J- and H-bands. In contrast to the situation at the TIRGO (an IR–optimized telescope at a colder site), it was possible to correct the photometry in K using differential dome flats, that is the difference between a uniformly-illuminated scene and the same scene without illumination (e.g., McCaughrean 1989). Whereas we divided by the sky frame to flat-field an image acquired at the TIRGO, at the WHT we needed to first subtract the sky frame and then apply the flat-field correction with differential flat fields. Since this operation was necessary only in the K-band, we hypothesize that the WHT, because of heavy baffling, is more emissive than the TIRGO, and produces a background in the K-band that is not spatially uniform. The background consists of atmospheric emission plus the emission from the telescope structure; hence sky frames are not suitable for the flat field correction.

At the WHT, by first subtracting a sky frame, then using differential dome flats for the flat field correction, spatial variation in the photometry was reduced by more than a factor of two; peak-to-peak variation went from 20% to 8% and the standard deviation with position was reduced to less than 3%. The empirical correction necessary for the TIRGO commissioning data was not needed to achieve this result.

6.2 TIRGO, February, 1994

For the subsequent observing campaign at the TIRGO (February, 1994), we altered the camera optics relative to those used during commissioning the year before: the cold stop at the pupil plane was eliminated as described in §2. This alteration was performed because of our hypothesis that the spatial variation in the photometry was caused by vignetting at the pupil plane of the camera. Such an effect can be due to an under-dimensioned cold stop, a badly positioned cold stop, or both. We acquired data in the same two modes as those of the commissioning run, namely five-position frequent standard star observations and 64-position 8×8 grids, and reduced the images as before.

Results support the hypothesis of pupil image vignetting. The same methods used to correct for this effect in the commissioning data were applied to the photometry of February, 1994; the results are shown in Table 6. Before application of any empirical correction, spatial variation of the photometry was comparable to the photometric quality of the night (4–8%), as assessed by repeated observations of standard stars. As can be seen from the table, unlike the commissioning data, application of the correction did not improve the spatial variation of the photometry.

7 Results obtained with ARNICA

A number of observing projects have been initiated with ARNICA's commissioning and are currently underway. These include studies of the comet P/Schaumasse during the pre- and post-perihelium phases (Tozzi et al. 1993); the embedded population around Herbig Ae/Be stars (Testi et al. 1994a; Figure 5); water masers associated with young stars and CO outflows (Palla et al. 1994; Hunter et al. 1994; Testi et al. 1995; Figure 6); star formation in S155 and the Cepheus B region (Hunt et al. 1993; Testi et al. 1994b; Figure 7); Cepheid variables in nearby galaxies (Piotto et al. 1994); the structure of early type spiral galaxies (Moriondo et al. 1993; Moriondo 1994; Figure 8); morphology of spiral galaxies and large scale structure (Baffa et al. 1994; Gavazzi et al. 1994; Figure 9); variability in Seyfert 1 galaxies (Hunt et al. 1994c; Figure 10); and distant radio galaxies (Borelli et al. 1994; Figure 11).

The capability of ARNICA mounted on a 4-m class telescope is illustrated in Figure 12 which shows an H-band image of the most distant known galaxy, 4C41.17 ($z = 3.8$), acquired by di Serego et al. during the December, 1993 observing run at the WHT. The observed limiting point-source H-magnitude or detection limit for this image is 21.2 (3σ, $1.3''$ FWHM) in 22.5 minutes of integration time on-source. The target object is clearly visible ($m_H = 19.7$) in the gaussian-convolved image (bottom panel).

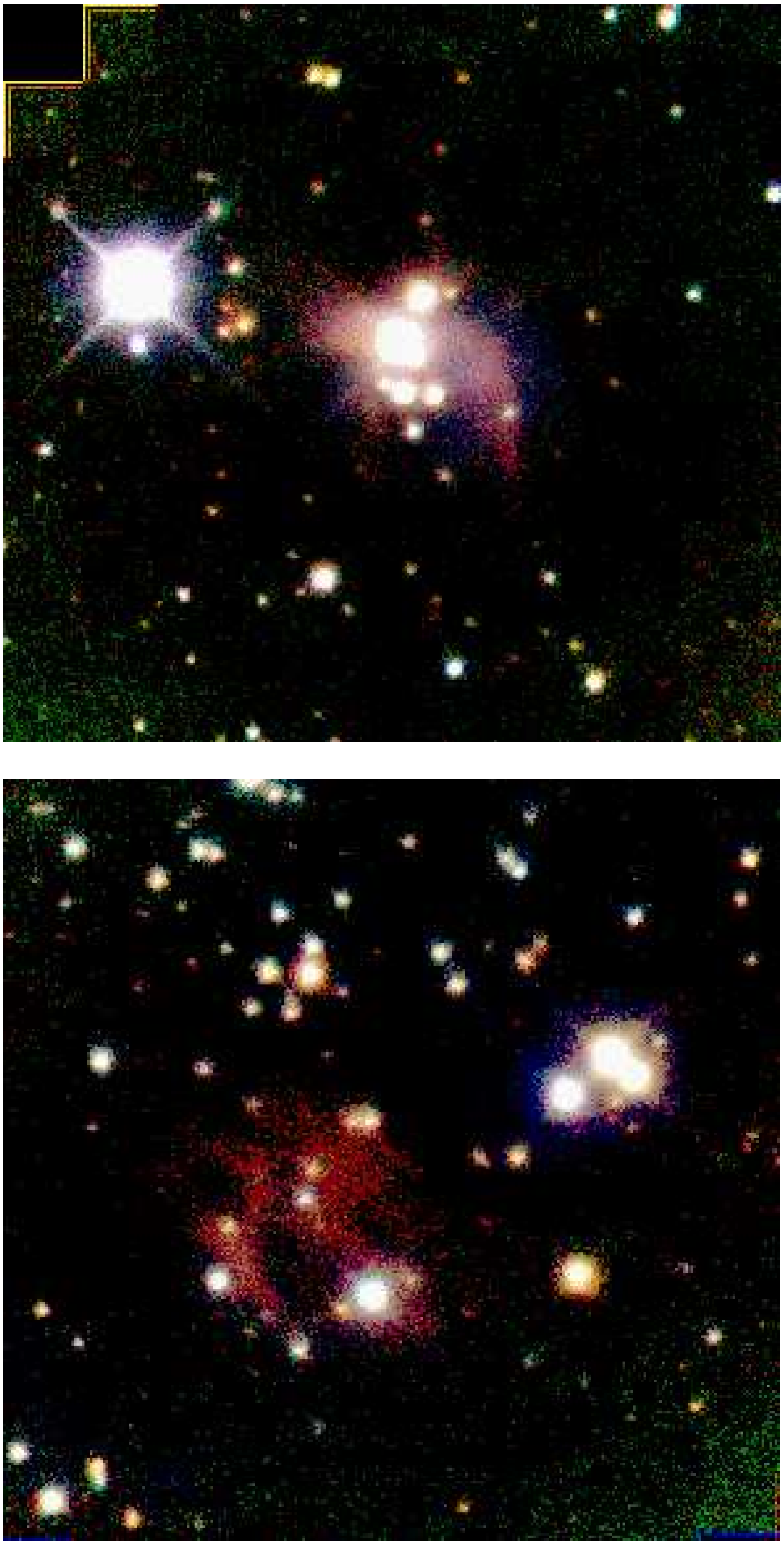

Figure 5: "True-colour" images of LkHα 215 (top panel) and LkHα 25 (bottom panel). Project: The embedded population around Herbig Ae/Be stars (Testi et al. 1994a).

8 Concluding remarks

ARNICA has proved to be a sensitive and reliable instrument, whose performance has far surpassed our expectations. After the first year of observing with ARNICA, the problem of spatial variation of the photometry seems to have been solved; the hypothesis of vignetting of the pupil image seems to be consistent with the results obtained. Future work includes a systematic determination of ARNICA's astronomical performance with the narrow-band filters; an analysis with optical design codes of the effects of pupil image aberration; and more complex read-out algorithms to enable rapid photometry and sub-array imaging.

9 Acknowledgements

We would like to thank F. Lisi, C. Baffa, D. Bonaccini, S. Gennari, E. Oliva, and R. Stanga for interesting discussions and insightful comments, as well as the staffs at the TIRGO and the WHT for making the observing campaigns run smoothly.

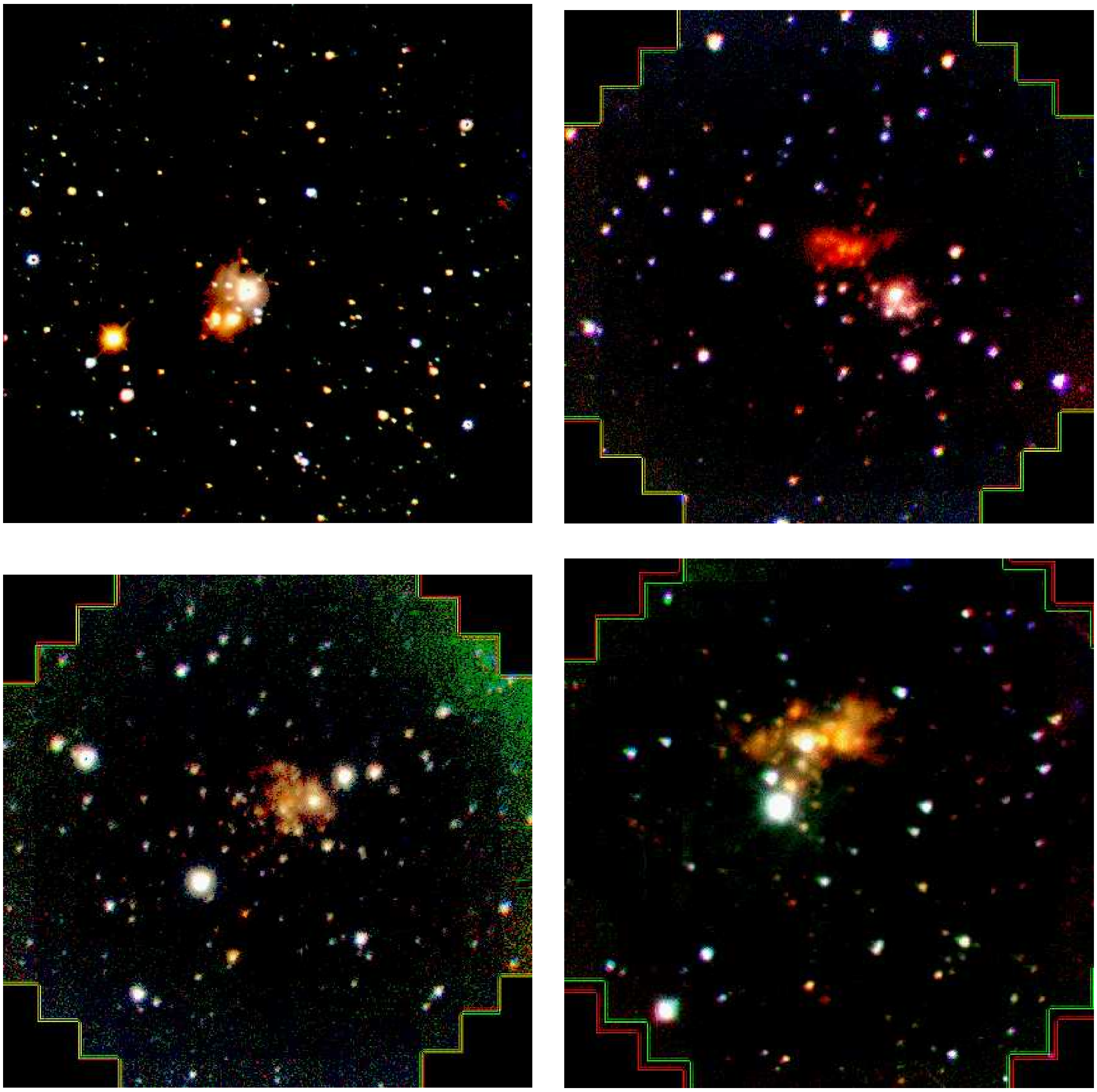

Figure 6: "True-colour" images of H_2O maser and CO outflows. Clockwise from upper left: BD+40°4124, S 233, AFGL 5180, and AFGL 5142. Project: Exploring the engines of molecular outflows (Palla et al. 1994; Hunter et al. 1994; Testi et al. 1995).

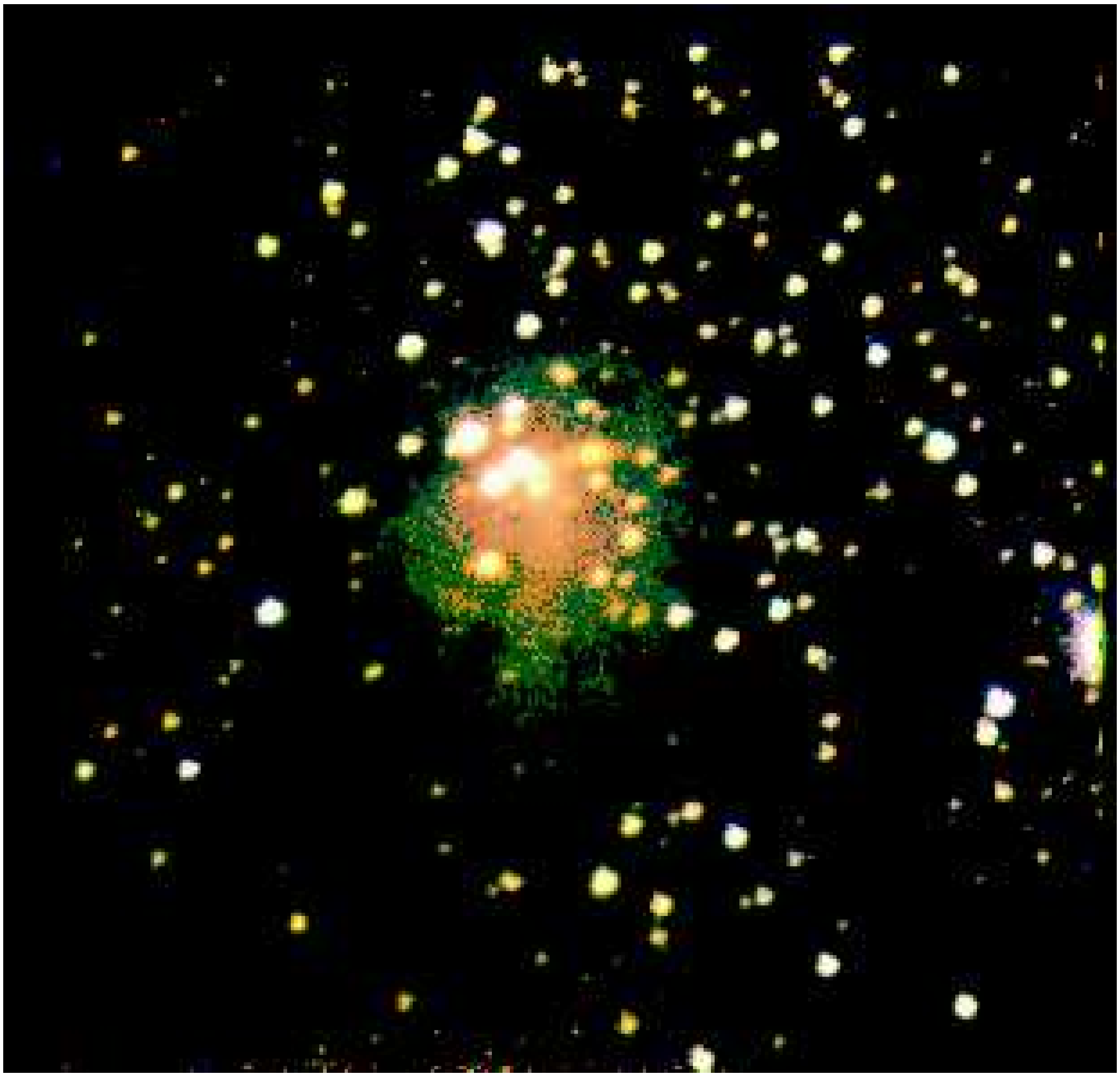

Figure 7: "True-colour" image of the S155/Cepheus B interface. Project: Stimulated star formation (Hunt et al. 1993; Testi et al. 1994b).

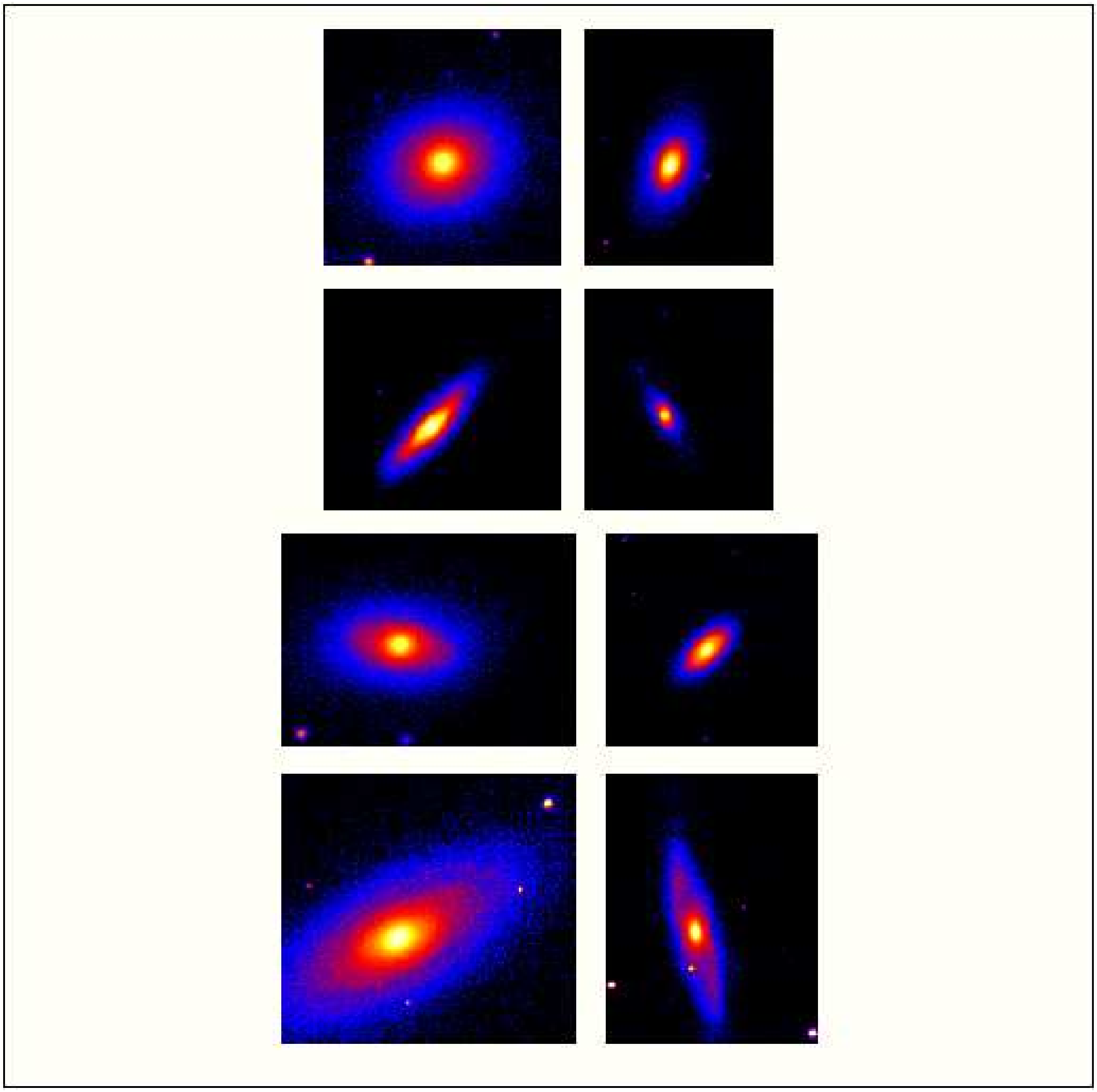

Figure 8: K-band images of early-type spiral galaxies. Clockwise from upper left: NGC 2775, NGC 3898, NGC 724, NGC 2639, NGC 4845, NGC 2841, NGC 4450, and NGC 4419. Project: Quantitative morphology of early-type spirals (Moriondo et al. 1993; Moriondo 1994).

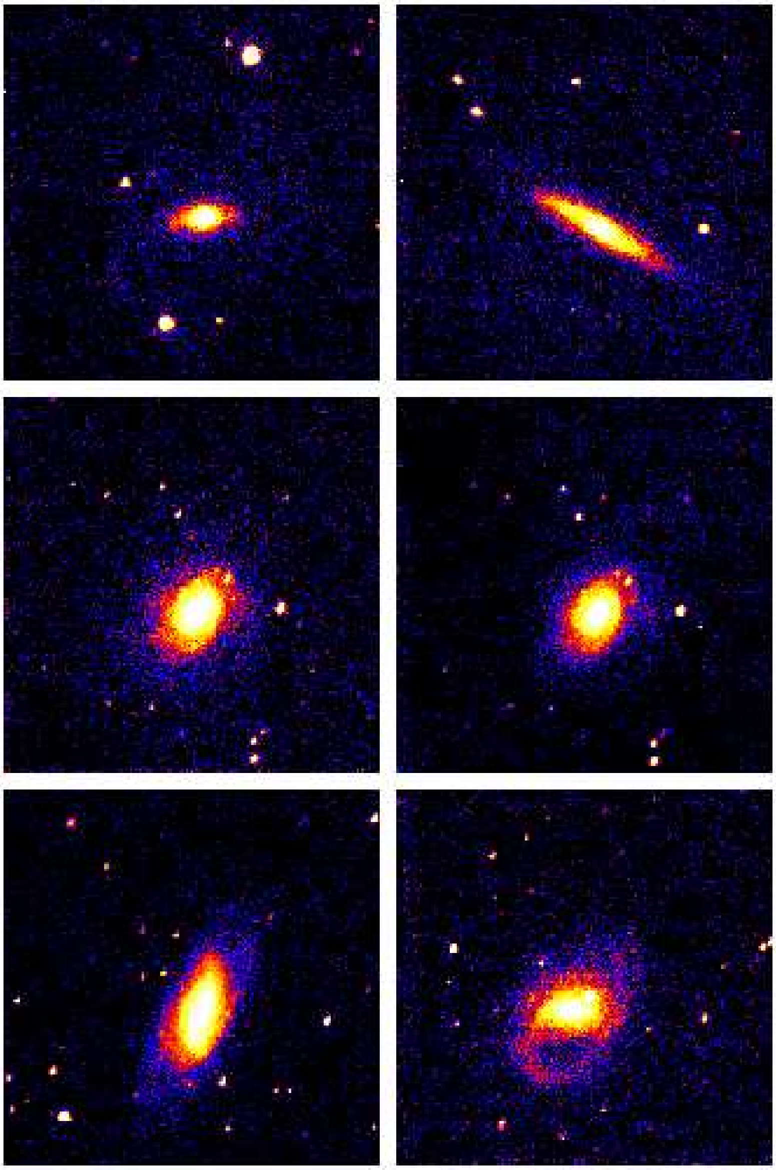

Figure 9: H- and K-band images of normal spiral galaxies. Clockwise from upper left: UCG 12776 (H), UGC 1205 (H), NGC 753 (H), NGC 1207 (K), NGC 818 (K), and NGC 753 (K). Project: NIR images of normal spirals (Baffa et al. 1994; Gavazzi et al. 1994).

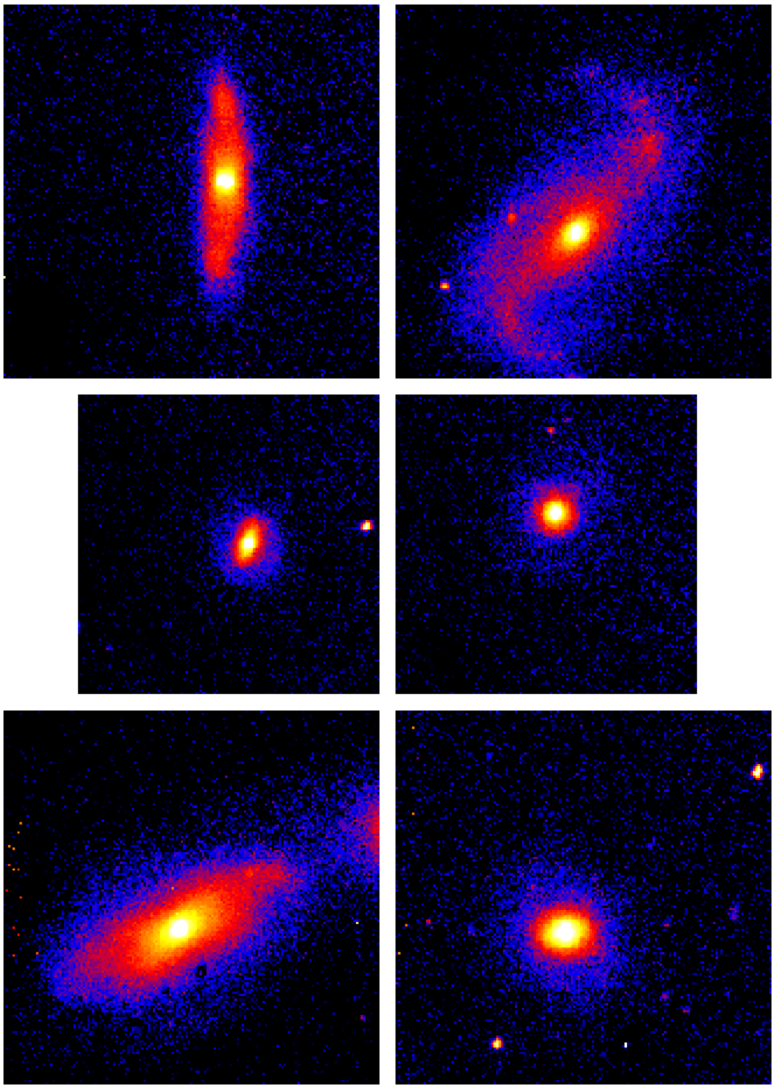

Figure 10: K-band images of X-ray selected Seyfert 1 galaxies. Clockwise from upper left: NGC 5506, NGC 4051, NGC 5548, NGC 3516, NGC 3227, and Mkn 766. Project: Limits on the short-timescale near-infrared variability in Seyfert 1 nuclei (Hunt et al. 1994c).

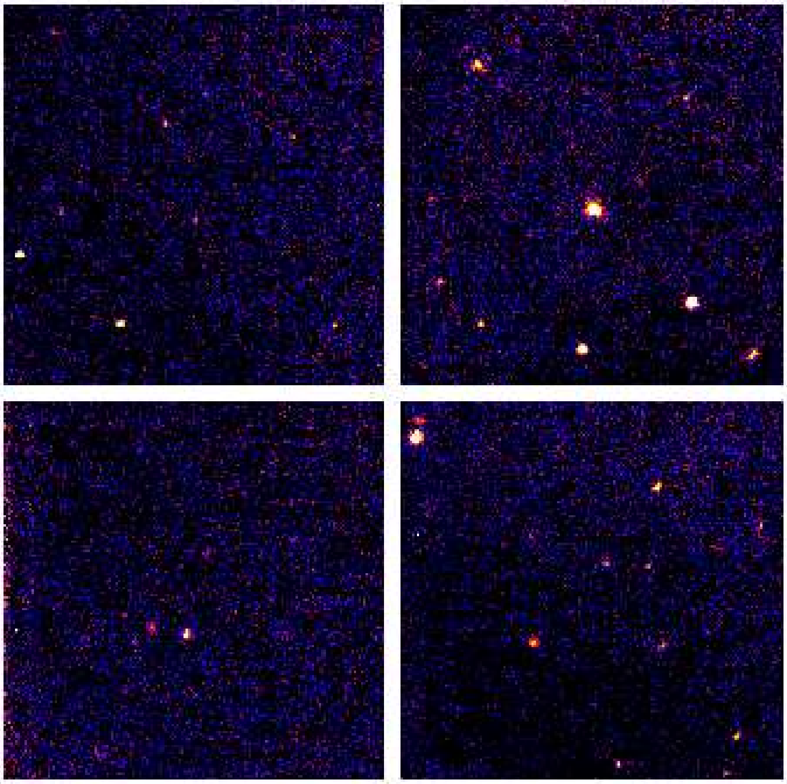

Figure 11: K-band images of distant radio galaxies. Clockwise from upper left: 0903+42, 3C223.1, 0956+47, and 3C234.0. Project: Infrared studies of distant radio galaxies (Borelli et al. 1994).

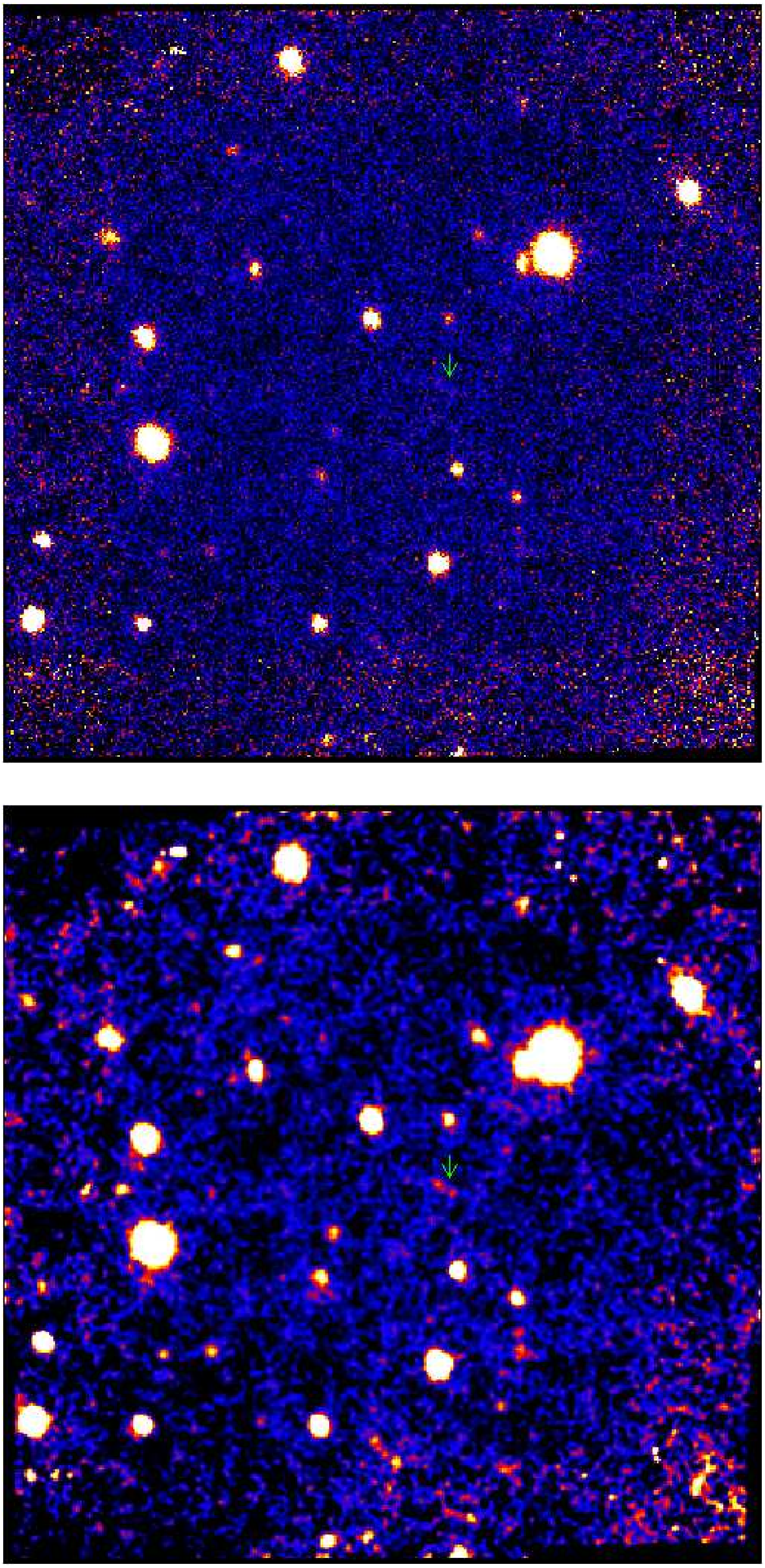

Figure 12: WHT H-band image of 4C41.17 of the most distant known galaxy (di Serego Alighieri et al. 1994). The galaxy is indicated with an arrow. The top panel shows the image after standard data reduction; the bottom panel shows the reduced image convolved with a two-dimensional gaussian function.

References

Baffa, C. et al. 1994, in preparation

Borelli, S. et al. 1994, in preparation

Campins, H., Rieke, G.H., & Lebofsky, M.J. 1985, AJ, 90(5), 896

Carter, D. 1993, Gemini, No. 39, 14

Esposito, S., Brusa, G., Bonaccini, D., & Ranfagni, P. 1993, Arcetri Observatory Technical Report N. 9/93.

Gavazzi, G. et al. 1994, in preparation

Gennari, S. & Vanzi, L. 1994, Arcetri Observatory Technical Report N. 8/94.

Henden, A.A. & Kaitchuck, R.H. 1982, *Astronomical Photometry*, Van Nostrand Reinhold Company, New York

Hillenbrand, L.A., Strom, S.E., Vrba, F.J., & Keene, J. 1992, ApJ, 397, 613

Hunt, L.K. 1993, Laurea Thesis, University of Florence

Hunt, L.K., Lisi, F., Felli, M., & Tofani, G. 1993, Proceedings of the 2nd Köln-Zermatt Symposium, The Physics and Chemistry of Interstellar Molecular Clouds, Zermatt, September

Hunt, L., Maiolino, R., & Moriondo, G., 1994a, Arcetri Observatory Technical Report N. 2/94 (Report I).

Hunt, L.K., Testi, L., Borelli, S., Maiolino, R., & Moriondo, G. 1994b, Arcetri Technical Report, N. 4/1994 (Report III).

Hunt, L.K., Salvati, M., Zhekov, S., Mannucci, F., & Stanga, R.M. 1994c, A&A, in press

Hunter, T.R., Testi, L., Taylor, G.B., Tofani, G., Felli, M., & Phillips, T.G. 1994, A&A, submitted

Lisi, F., Baffa, C., & Hunt, L. 1993, "ARNICA: the Arcetri Observatory NICMOS-3 imaging camera", Proceedings of SPIE Technical Conference 1946, Orlando

McCaughrean, M.J. 1988, Ph.D. Thesis, University of Edinburgh

McCaughrean, M.J. 1989, in Proceedings of the Third Infrared Detector Technology Workshop, ed. C.R. McCreight, NASA Technical Memorandum No. 102209, p.201

Moriondo, G., Hunt, L., Baffa, C., Giovanardi, C., Lisi, F., & Stanga, R. 1993, in Proceedings of Infrared Astronomy with Arrays: the Next Generation, UCLA, in press

Moriondo, G. 1994, Laurea Thesis, University of Florence

Palla et al. 1994, A&A, in press

Persson, S.E., West, S.C., Carr, D.M., Sivaramakrishnan, A., & Murphy, D.C. 1992, PASP, 104, 204

Piotto, G.P. et al. 1994, in preparation

Rieke, M.J., Rieke, G.H., & Montgomery, E.F. 1987, in Infrared Astronomy with Arrays, eds. C.G. Wynn-Williams and E.E. Becklin, University of Hawaii, 213

Testi, L., 1993, Arcetri Technical Report N. 10/1993

Testi, L., Stanga, R.M., Natta, A., Palla, F., Prusti, T., Baffa, C., Hunt, L.K., & Lisi, F. 1994a, in Proceedings of the First conference on the nature and evolutionary status of Herbig Ae/Be stars, eds. P.S. Thè, E. van de Heuvel, and M. Perez, ASP Conference Series, Vol. 62, 355

Testi, L., Olmi, L., Hunt, L., Tofani, G., Felli, M., & Goldsmith, P. 1994b, in preparation

Testi, L. et al. 1995, in preparation

Tozzi, G.P., Baffa, C., Di Giacomo, A., Lisi, F., Hunt, L., & Stanga, R. 1993, in the Proceedings of the IAU Symposium 160 on Asteroids, Comets, and Meteors, Belgirate, in press

Wilson, W.J., Schwartz, P.R., Neugebauer, G., Harvey, P.M., & Becklin, E.E. 1972, ApJ, 177, 523